ASTRONOMY AND ASTROPHYSICS

Internal turbulence, viriality, and density bounding of the most luminous H II regions in the spiral galaxy M 100

M. Rozas[1], **N. Sabalisck**[1], **J.E. Beckman**[1], **and J.H. Knapen**[2]

[1] Instituto de Astrofísica de Canarias, E-38200 La Laguna, Tenerife, Canarias, Spain (mrozas, nss, jeb@iac.es)
[2] University of Hertfordshire, Department of Physical Sciences, College Lane, Hatfield, Herts AL10 9AB, UK (knapen@star.herts.ac.uk)

Received 20 May 1998 / Accepted 2 July 1998

Abstract. We present TAURUS Fabry-Perot velocity data in Hα emission of the disc of the grand design spiral M 100 (NGC 4321). We have studied the emission spectra of the 200 H II regions most luminous in Hα, calibrated in luminosity using photometric Hα imaging from the literature. The emission spectra of individual H II regions were fitted using one or more Gaussian functions, and analyzed in terms of their velocity dispersion. We concentrate on the question of whether the emission lines show values of their internal velocity dispersions of H II regions which would be predicted from the virial theorem, and find that in general this is not the case. There is a systematic trend to super-virial line widths, characteristic of the non-equilibrium effects of powerful OB stellar winds, and supernovae. We propose that the lower envelope in velocity dispersion σ, in the plot of Hα luminosity v. σ represents the virialized regions, and give a tentative theoretical explanation for its slope of 2.6 in the log–log plane, in terms of density bounding for the regions of highest luminosity.

Key words: ISM: HII regions – galaxies: individual: M100 – galaxies: spiral – galaxies: structure – galaxies: ISM

1. Introduction

The use of the properties of the most luminous extragalactic H II regions as standard indicators of distance (Sersic 1960; Sandage 1962) is in principle very attractive. These regions are the brightest objects in a galaxy which are not ephemeral, and H II regions are present in all normal spiral galaxies. The emission fluxes in Hα , which can be higher than 10^{40} erg s^{-1} and the sizes of these regions, some hundreds of pc in diameter, imply that they can be observed well into the Hubble flow. The fact that they are significantly less bright than supernovae is at least partially offset by their ready availability for careful observation and analysis.

One of the properties which has been used in the past is, in fact, the diameter as a function of luminosity, (Sandage & Tammann, 1974) but this suffers from the drawback that the diameter of an H II region depends not only on the properties of its ionizing stars, but also on the properties of the surrounding interstellar medium, which gives a probable two-parameter dependence. Also, measuring the observed diameter against the background of emission in the same line (nowadays normally Hα) gives a notoriously uncertain value, since the edges of a projected H II region are always the faintest parts of the region, and to define them can in practice be an almost arbitrary exercise in photometric definition.

Another parameter which has been used (Kennicutt 1979a, b, c; van den Bergh, 1980) is a statistical property: the luminosity of the n^{th} brightest region, but as Kennicutt (1981) himself later pointed out, if n is small enough for the region in question to be of high luminosity, there is a large variation in this value, which goes with the observation that the luminosity of the most luminous region shows rather large variations from one galaxy to another (Hanes, 1982). This is not surprising, since there is a plausible physical relation between the mass of a galaxy, and the masses of its most massive gas clouds, and between these masses and the luminosities of the most massive stars, and hence of the most luminous H II regions. If n is large enough for this effect to be smoothed out, the corresponding regions will be too faint to observe with good photometric precision, and in any case this luminosity will be an intrinsic function of that of the parent galaxy. For this reason these methods were set aside as reliable distance indicators, following a detailed examination of the problem by Hanes (1982).

In a recent paper (Beckman et al. 1998) we showed that a parameter which should be affected only to second order by variation in the galaxy mass is the luminosity of the transition between ionization bounded and density bounded H II regions, which occurs in Hα at a luminosity of $L_{\rm Str} = 10^{38.6}$ erg s^{-1}. This value is observed to vary very little from galaxy to galaxy, as predicted. The transition is recognizable via the change in slope, accompanied by a local maximum, in the H II region luminosity function at this critical luminosity. If we take into account the hypothesis that the regions with higher luminosity than this are density bounded, we should find that their observed properties follow different relations from those predicted for ionization bounded regions (Beckman et al. 1998).

One of these relations is that between luminosity and internal velocity dispersion. Melnick (1978) found a strong correlation between the absolute magnitude $M_{\rm B}$ of a galaxy and the velocity dispersion of its most luminous H II regions , and in a study

Send offprint requests to: J.E. Beckman

carried out in the early 1980's via Hβ (favoured then for reasons of detector sensitivity) Terlevich and Melnick (1981) claimed to find that the Hβ luminosity of the most luminous H II regions varies as the 4th power of the measured velocity dispersion. They believed that this result showed that the most luminous H II regions are virialized, so that information about their masses, and the resultant mass-luminosity relation, could be obtained using the virial theorem. They also claimed a relation between a radius parameter R and the square of the velocity dispersion σ for H II regions, as further evidence for virialization. However in one of the few complete statistical studies of velocity dispersions in H II regions within any galaxy, Arsenault et al. (1990) gave observational results for M 100 which in no way approximate to a 4th power relation between L and σ. Their results are more correctly termed a pure scatter diagram, in which the velocity dispersion does not even rise systematically with increasing H II region luminosity.

In the context of our systematic study of the statistical properties of H II regions in external large spirals, we chose to observe M 100 using a two-dimensional Fabry-Perot technique, similar to that employed by Arsenault et al. (1990). The galaxy was in fact chosen because we had already published a number of studies of its disc and of its circumnuclear zone using broad-band photometry in the visible and near infrared (Knapen et al. 1995a,b; Knapen & Beckman 1996; Beckman et al. 1996) as well as H I 21 cm mapping (Knapen et al. 1993) and partial mapping in CO (Cepa et al. 1992; Knapen et al. 1996). The velocity field in Hα could serve both as a kinematic diagnostic for the circumnuclear zone (Knapen 1996) and to provide new high quality observations of the disk H II regions. The analysis of these latter data form the subject of the present article.

In Sect. 2 we briefly describe the observation and reduction technique, and explain the different types of two-dimensional information available in the form of intensity and kinematic maps. In Sect. 3 we show how the emission spectra of the individual H II regions were obtained, explaining how multiple components, which occurred for many of the regions, were separated both spatially and in wavelength, so that our understanding of what is occurring in a region may be enhanced compared with the work of Arsenault et al. (1990). In Sect. 4 we examine the observational relationship between the luminosity L and the velocity dispersion σ of the regions, and in Sect. 5 we give a physical explanation of these observations, not only taking fully into account the physical implications of the fact that the high luminosity regions are density bounded, but using an implied model of how the internal motions within a region are stimulated in order to explain some of the features of the $L - \sigma$ plot. In Sect. 6 we draw our general conclusions about the use, and the limitations of the virial theorem in inferring the masses of H II regions.

2. Observations and data redution

The observations of M 100 were obtained using the TAURUS II Fabry-Perot imaging spectrograph at the Cassegrain focus of the 4.2m William Herschel Telescope, La Palma, during May 1995. The night was photometric with $\sim$0.7 arcsec seeing. The detector was a TEK CCD. The observations consisted of a scan in wavelength, and by implication velocity, through the Hα emission line across the face of the galaxy. The TAURUS II system gives, as its final data product, a "cube" of data, whose dimensions are the two spatial dimensions on the sky, and the wavelength. The Hα intensity at each point in this three-dimensional grid is the stored variable. The size of the cube was, in this case, 600 pixels $\times$ 600pixels $\times$ 55 "planes" in wavelength. The spatial scale is 0.28 arcsec pixel^{-1}, and in the spectral direction the wavelength interval between planes is some 0.34 Å, which corresponds to 15.5 km s^{-1}. The total velocity range employed corresponds to the free spectral range of the interferometer: 17.9 Å, or 819 km s^{-1}. The exposure time was 140 s per plane.

Wavelength and phase calibration were performed by observing a calibration lamp before and after each science exposure. We used TAUCAL (FIGARO is the softwere environment in which TAUCAL runs) to convert the raw data, where surfaces of constant wavelength are in fact paraboloids, to cartesian cubic coordinates. We observed NGC 4321 (M 100) at two offset positions, since the galaxy is too big to fit into the TAURUS field. The region of overlap included the centre of the galaxy, and the two data sets were shifted spatially and combined by comparing the positions of foreground stars and well-defined H II regions occurring in both. Astrometry was performed by comparison with the Hα image of Knapen (1998), which, due to its larger angular size, contains a sufficient number of foreground stars to obtain a good astrometric solution. We estimate that the astrometric accuracy of positions in the data set presented here is 0.5 seconds of arc. The final, reduced data cube is presented in Fig. 1, where we plot the intensity of a number of velocity planes in the data set in a manner equivalent to the classical "channel maps" in radioastronomy.

3. Results

3.1. Total intensity, velocity, and velocity dispersion maps

Whereas channel maps, as in Fig. 1, serve to summarize especially global information about changes in the emitting wavelength across the face of the galaxy, a more detailed spatial description of intensities and velocities is given by moment maps. Fig. 2 shows the zero-th moment, or total Hα intensity, map of M 100. The map was produced by first extracting the emission line spectrum at each (RA, dec) point, which is then fitted with a single gaussian, for which the fitting program (MOMENTS in GIPSY) yields values for the integrated intensity, central wavelength (or radial velocity), and velocity dispersion. Only emission occurring at the same position in at least three adjacent channels was considered true signal, and used for the calculation of the moment maps.

In making the moment maps we neglected the fact that the best fit might not comprise a single gaussian (for further details see Sect. 3.2), since we were concerned only to find the global distribution of peak intensity, and the galaxy-wide velocity field and dispersion distribution. It is necessary to note here that the

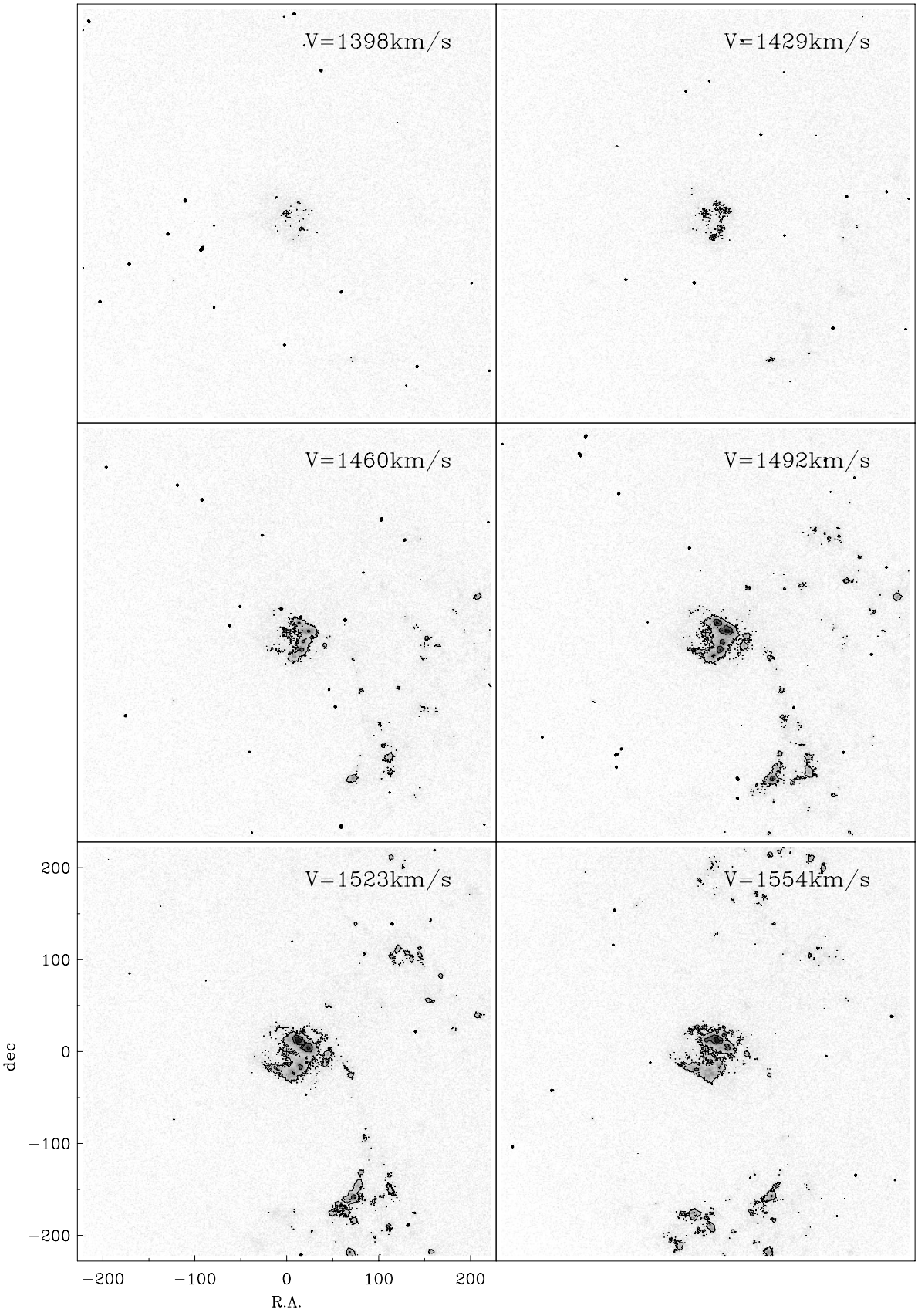

Fig. 1. Planes of the Hα data cube for NGC 4321 at a series of velocities about the central systemic value of 1540 km s^{-1}.

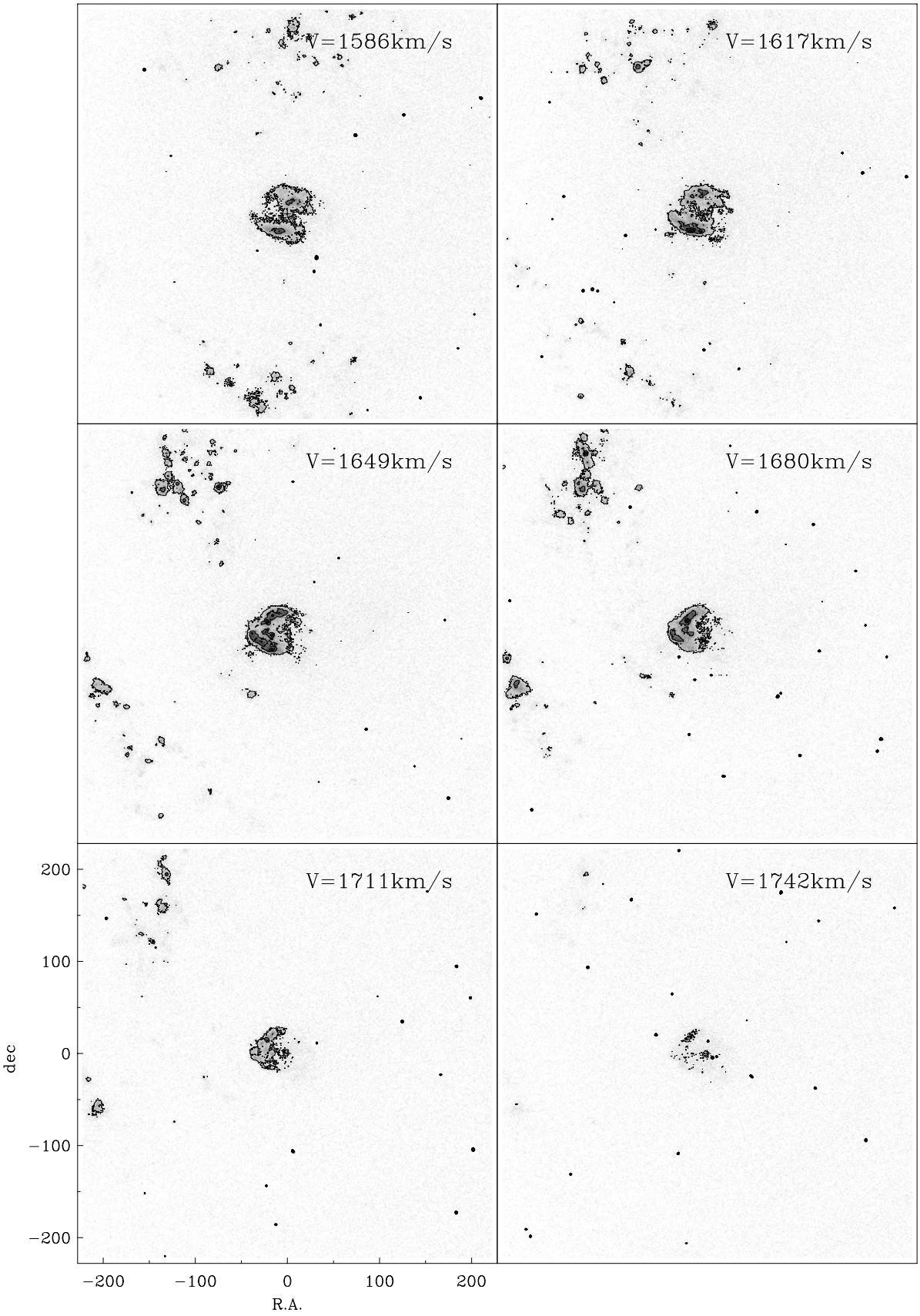

Fig. 1. (continued)

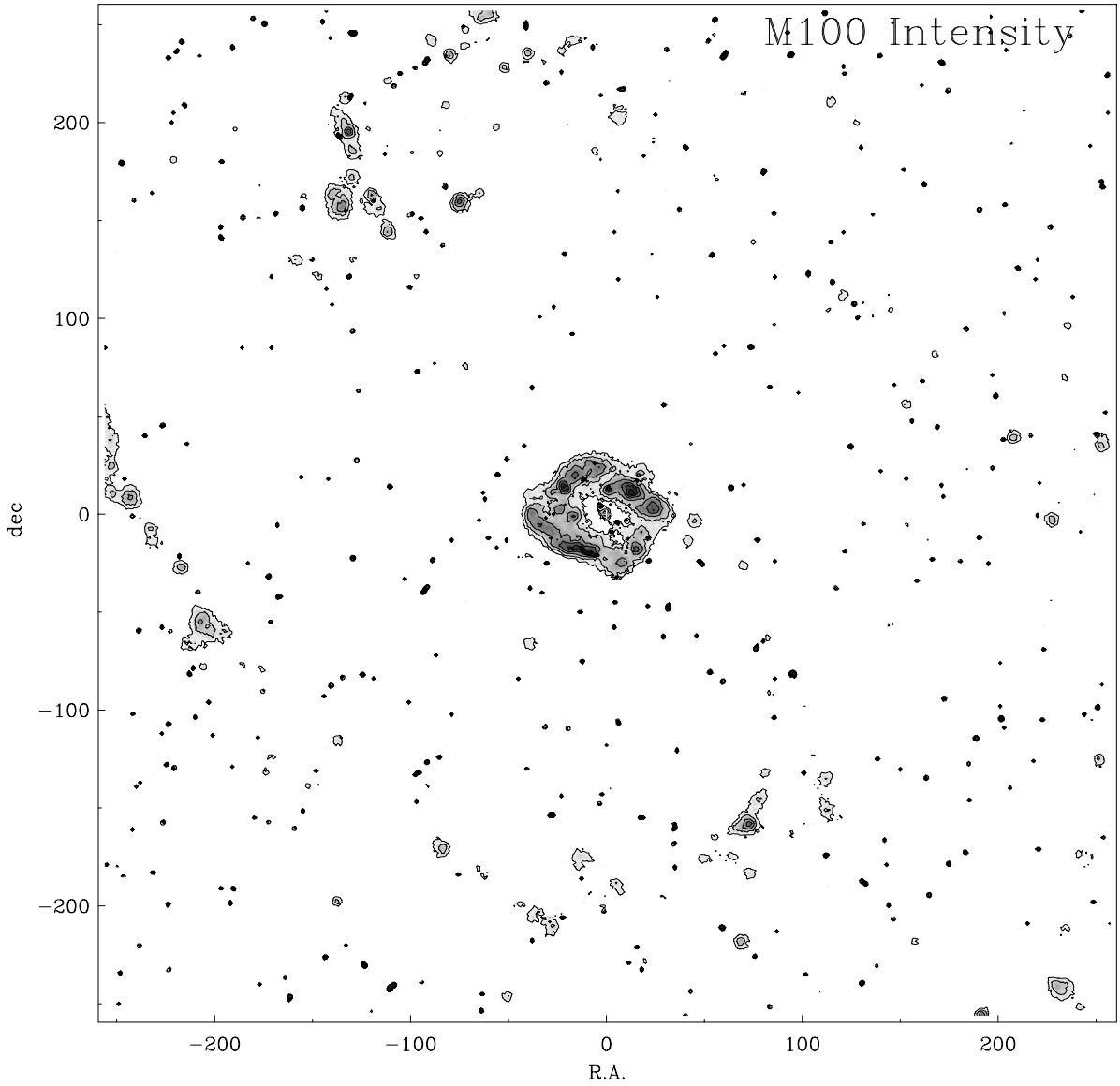

Fig. 2. Map of the integrated Hα emission intensity in NGC 4321 from the TAURUS observations described in the present paper. Contour levels are at 0.5, 2.0, 8.0, 24.0, 40.0 $\times$ 10^{36} erg s^{-1}.

total intensity Hα map presented here in Fig. 2 does not go as deep as straight intensity maps of galaxies in Hα taken through interference filters. Taking the present case as an example, the intensity map shown in Fig. 2 shows less than 200 H II regions in the disc of M 100, whereas a recent mapping exercise using the same telescope and camera optics, but through an interference filter only and mosaicing four fields, thus covering the complete disc of the galaxy shows just under 2000 H II regions (Knapen 1998). In the present article, we are necessarily confined to information from the most luminous regions, most of which are found in the spiral arms and the circumnuclear zone of enhanced star formation.

In Fig. 3 we present the first moment map, showing the global velocity field of the Hα emitting regions across the face of the galaxy, obtained using the peak wavelength of the single gaussian fit for each pixel, as described in the previous paragraph. The resulting map gives a good overview of the global kinematics of the galaxy, as further discussed by Knapen et al. (1998).

The velocity dispersion is the final global property for which we show a moment map (second moment) of the central part of the galaxy (Fig. 4). The map is not purely observational, giving the value of the dispersion corrected for both the instrumental width and the thermal velocity width of the ionized gas. The former has the value 18.4 km s^{-1}, and to obtain the dispersion due to internal turbulence alone, we adopted a standard value for the thermal broadening corresponding to an H II region with a temperature of 10^4 K. To find the turbulent velocity dispersion we subtracted the instrumental dispersion and the thermal dispersion in quadrature from the observed width. A mean, rep-

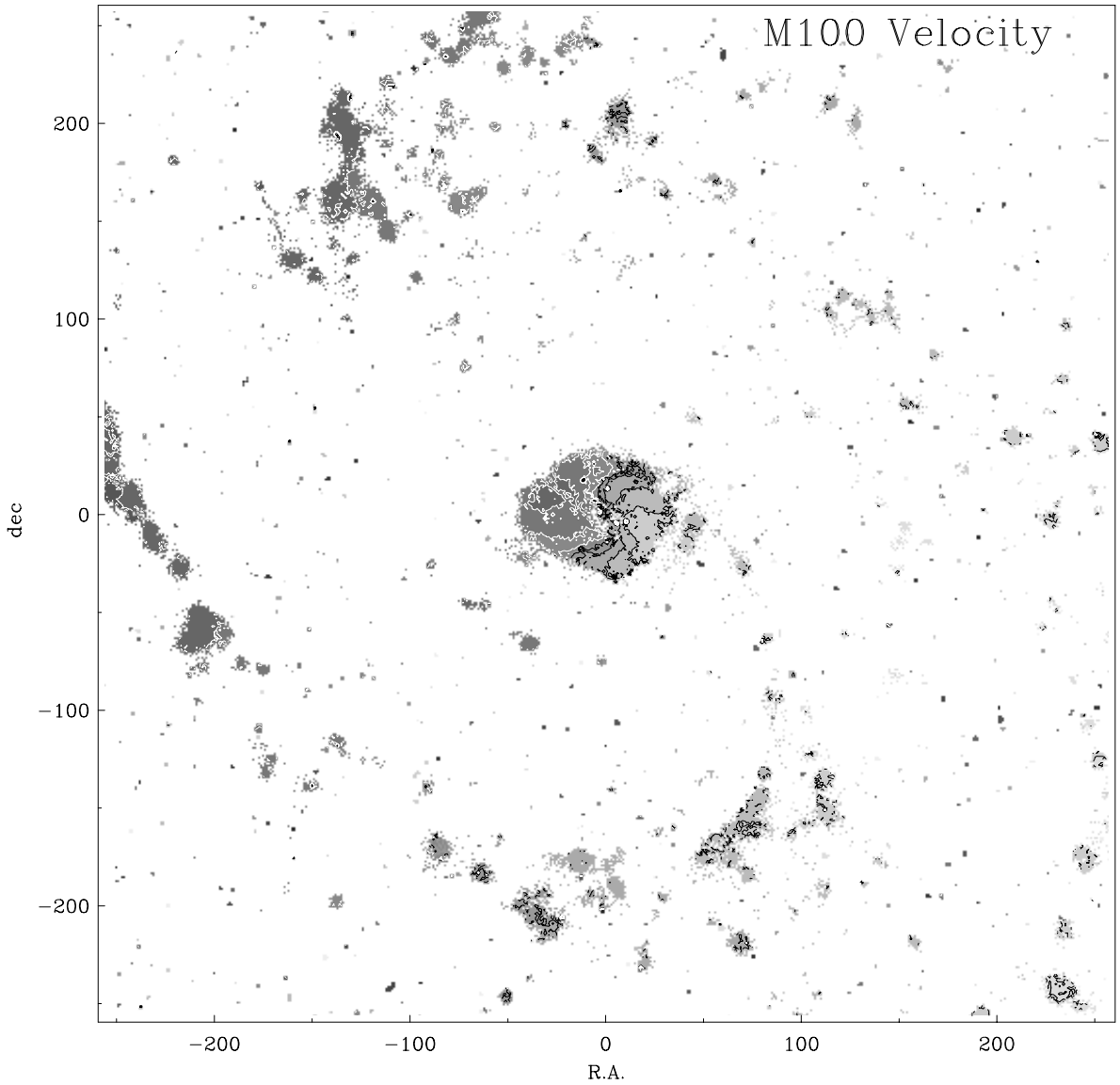

Fig. 3. Map of the peak radial velocity of Hα as a function of position across NGC 4321. Contour levels are situated at 1420, 1450, 1480, 1510, 1540, 1580, 1610, 1640, 1670, 1700, 1730 km s^{-1}.

resentative value of the turbulent width σ is 20 km s^{-1}. We note once more that in the process of extracting the dispersions we have made no attempt to split the lines into components, so that the dispersions obtained are in some cases the result of the blending of multiple components in a given position on the galaxy. These details will be examined below.

3.2. Spectral analysis

The most complete information about a localized region of the galaxy is obtained via point by point spectra giving pixel by pixel line profiles, which can be grouped according to the situation of the pixels, the most obvious example being to integrate over a single H II region. We select a prescribed zone, defined by a square grid of pixels of given dimension, and within this zone, carry out an averaging process of the intensities in the individual velocity planes. We thus obtain a spectrum of the zone, which is subsequently analyzed in terms of a set of gaussians.

From the intensity map in Fig. 1 we first identify the separate H II regions, and estimate their sizes. We then apply the above routine systematically to a given region, starting from a central zone of minimum size, defined via the seeing as 3 × 3 pixels, which corresponds to some 1 arcsec on the sky, and stepping outwards in intervals of 2 × 2 pixels, until the whole region is included. At each step a spectrum is obtained, and these can be compared, to better understand the geometry of any of the gaussian components observed. The largest of the regions examined in this way subtended 19 × 19 pixels.

The spectrum obtained from the maximum area scanned, for a given H II region, we term the integrated profile of the

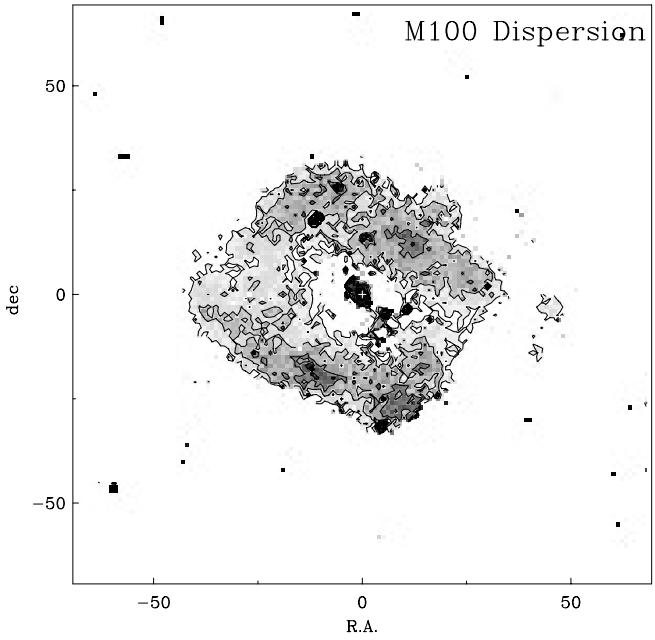

Fig. 4. Map of the velocity dispersion in Hα of the central part of the NGC 4321. The contours are situated at 20, 35, 50 and 65 km s^{-1}.

region. The regions show quite a wide variety of emission line profiles, and here we pick out only the salient properties. In many of the spectra obtained through the minimum aperture placed on the centre of a given H II region, the emission line was symmetric: virtually a gaussian. However in some of the brightest regions we find asymmetric spectra, even in the middle of a region, and in the centres of some regions we find a low intensity, high velocity dispersion component: the intensity may be some 10 % to 20 % of that of the principal component, but the velocity dispersion can reach as high a value as 80 km s^{-1}. On enlarging the aperture, there is a trend to encounter more asymmetries which imply separate components each with a different velocity dispersion. With the biggest regions these asymmetries tend to blend away at very large apertures, leaving a sort of averaged symmetrical profile. In some cases, we are most probably sampling more than one region within the beam and cannot separate the different regions along the line of sight due simply to projection.

Quantitatively at least, this picture is in agreement with a recent detailed study of the giant H II region NGC 604 in M33 co-authored by one of us (Medina Tanco et al. 1997). These authors showed that within such a region there can be a number of separate sources of velocity dispersion, superposed on a general background within the region. Each separable source corresponds to a massive star, with a stellar wind, or to a supernova remnant. In M 100, such features cannot be expected to be identifiable spatially in even the largest H II regions, but their contributions to the line profile of the H II region of which they form part should be detectable spectrally.

Fig. 5 gives examples of spectra obtained from characteristic regions with different sample apertures, and is illustrative of the kinds of spectra which are observed. As well as the complete profiles we have included their analyses into separate components via sets of best-fit gaussians. The spectra and profile fits of all the H II regions considered here will be published electronically via the Centre de Données Stellaires (CDS) in Strasbourg.

4. Luminosity vs. velocity dispersion

The luminosities of the H II regions were obtained by comparing them region by region in the intensity map of Fig. 1 with the corresponding map in Knapen (1998), which was obtained also with the TAURUS camera, but without interferometry, i.e. by direct imaging. The latter is calibrated absolutely in Hα against standard stars, and as explained above is a much deeper image with far more regions visible, but is was not difficult to identify the 200 or so brightest regions we observed with the TAURUS Fabry-Perot system and thus use the calibration of Knapen (1998) to measure their luminosities.

The velocity dispersion we wish to examine is that due to the internal motions within an H II region. It was thus necessary to correct the observed dispersion $\sigma_{\rm obs}$ for the effects of natural line broadening, thermal broadening, and broadening due to the instrumental function, in order to obtain the kinematic, non-thermal broadening, $\sigma_{\rm nt}$. The expression used is:

$$\sigma_{\rm obs} = \left[\sigma_{\rm N}^2 + \sigma_{\rm Ins}^2 + \sigma_{\rm t}^2 + \sigma_{\rm nt}^2\right]^{1/2} \quad (1)$$

where the natural (quantum mechanical), instrumental, and thermal contributions to $\sigma_{\rm obs}$ are $\sigma_{\rm N}$, $\sigma_{\rm Ins}$, and $\sigma_{\rm t}$ respectively. The natural broadening is essentially a constant for hydrogen, and takes the value 0.16 Åwhich corresponds to 3 km s^{-1} (O'Dell & Townsley 1988). The instrumental width was found from our analysis of the calibration lines emitted by the laboratory source which we used to produce the data cube for the wavelength calibrations. The result of a careful analysis of the calibration cube showed that it contained no systematic structures due to calibration problems, and that the instrumental dispersion map showed a constant value of 18 ± 0.4 km s^{-1}, which we used as $\sigma_{\rm Ins}$. Computing a value for $\sigma_{\rm t}$ is standard procedure, since this is just the Doppler broadening of the emission line from the H II region. For H II regions with temperatures of 5000, 10000 and 15000 K, Osterbrock (1989) gives the corresponding values of $\sigma_{\rm t}$ as 6.4, 9.1 and 11.1 km s^{-1}.

In the absence of further detailed measurements for M 100 we adopted a uniform value for $\sigma_{\rm t}$ of 10 km s^{-1}; due to the quadratic relation required for the correction, errors due to variations in T from one region to another will never be greater than 2 km s^{-1}, and in general will be less than 1 km s^{-1}. However the estimate of the intrinsic rms error in $\sigma_{\rm nt}$ due to the scatter in the remaining components in Eq. 1 is of order 5 km s^{-1}, and we have included in our analysis only those lines or components which have inferred values of at least twice this value.

In Fig. 6 we show the luminosity L plotted against the velocity dispersion $\sigma_{\rm nt}$ for the principal components of the H II regions measured with TAURUS. The results form a rather broad-spread scatter diagram, and a quick inspection would lead one to believe that there was no deducible physical relation between

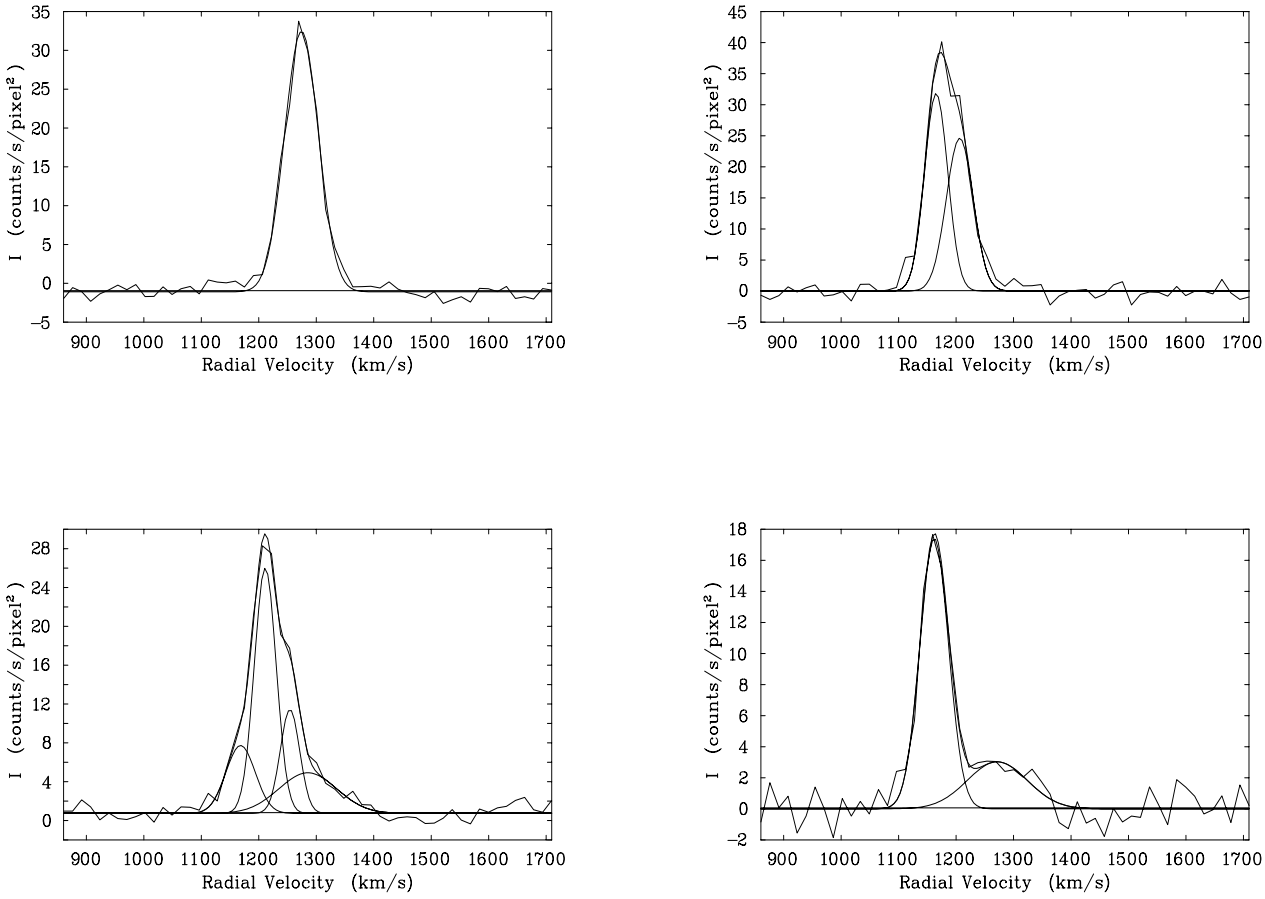

Fig. 5. Typical spectra observed: examples shown are a symmetric spectrum, an asymmetric spectrum, one with two principal components, and one with multiple components.

the two variables. However there are two trends which can be seen. Firstly there is a tendency for the scatter in σ, the interval between the extreme values at a given luminosity, to decrease with increasing luminosity; this scatter is greater in the zone round 10^{38} erg s^{-1} than at 10^{39} erg s^{-1} and above. In Fig. 6 this is seen principally as a trend to falling values of the highest $\sigma_{\rm nt}$ at a given luminosity as that luminosity increases. However noting the observational cut-off to low sigma it is probable also that the lowest values of $\sigma_{\rm nt}$ also increase with increasing L, a trend which is certainly seen above the cut-off at $\sigma_{\rm nt}$ = 10 km s^{-1}.

The second trend is the clean upper envelope to the plotted points, which we will comment on further below. At luminosities of 10^{38} erg s^{-1} and below there is an observational cut-off in the number of regions, but above 10^{39} erg s^{-1} the upper envelope is a real feature of the observations, which are statistically complete at those luminosities. The slope of the best linear fit to the envelope is 2.6 $\pm$ 0.14 It is interesting to compare this last result with a plot of the Hα fluxes versus velocity widths for those H II regions in M 100 with the highest surface brightnesses, observed using a similar Fabry-Perot technique to ours by Arsenault et al. (1990; their Fig. 12), in which a slope of 2.57 ± 0.49 was found. If the most luminous regions also are those with the highest surface brightness their result would be the same as ours, in that their H II regions would also lie along our upper luminosity envelope. The present result strongly suggests that this is so. However we can refer also to our recent paper (Rozas et al. 1998) in which we show that the surface brightness of H II regions as a population varies very little with luminosity for values of L below $L = L_{\rm Str} = 10^{38.6}$ erg s^{-1}, at which luminosity there is a jump to a higher value and a progressive increase thereafter. This result was found for a number of different spirals. We have offered a physical explanation for this transition in terms of the change from ionization bounding to density bounding at $L = L_{\rm Str}$. Here we simply point out that the equivalence of the most luminous regions to those of highest surface brightness is in full accord with the observational evidence. In Fig. 7 we have plotted the luminosity in Hα of only those regions showing fully gaussian profiles and whose velocity dispersions are supersonic. This selection criterion also yields an $L - \sigma$ dependence with a slope of 2.6 ± 0.2 and must be selecting a similar set of regions to those that were selected using surface brightness as the criterion by Arsenault et al. (1990).

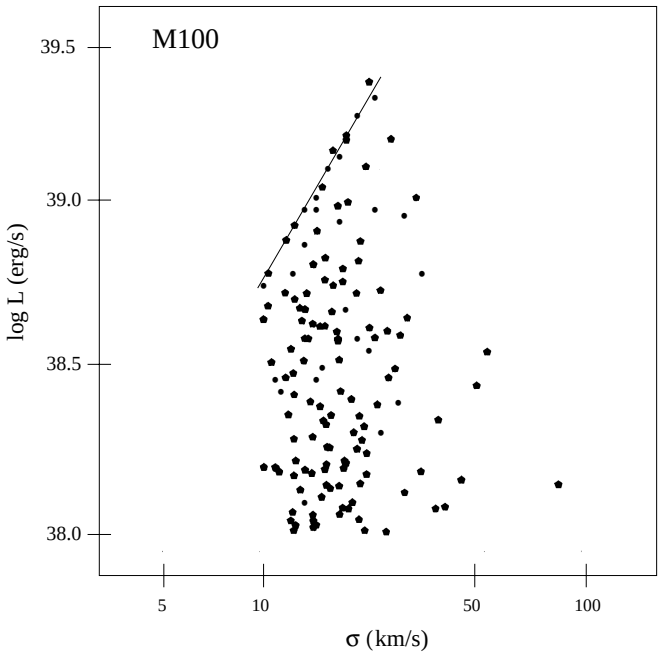

Fig. 6. Graph of the luminosity versus velocity dispersion for all the H II regions, using the principal components of each spectrum analyzed.

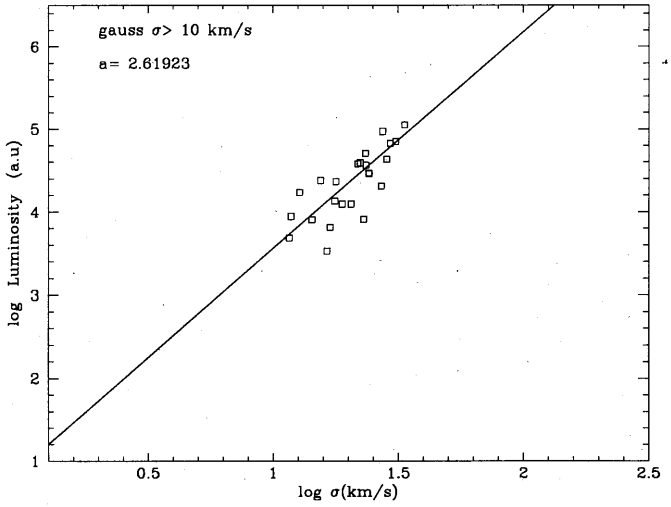

Fig. 7. Luminosity in Hα of those regions those spectra showing gaussian profiles and supersonic widths, versus the velocity dispersion of their integrated flux spectra.

5. Virialization of H II regions

Terlevich and Melnick (1981) proposed, on the basis of observations, that H II regions, above all the most luminous, the so-called "supergiant" H II regions, are virialized systems. They derive the relation between the Hβ luminosity of an H II region, $L_{\mathrm{H}\beta}$ (in erg s^{-1} and σ, as $\log L_{\mathrm{H}\beta} = 4.0 \log \sigma + 34.0$.

This relation is in line with what one would predict for gravitationally bound systems in virial equilibrium, and it would indeed be physically very interesting and useful if it were to hold. However, neither in the work by Arsenault et al. (1990) referenced above, nor in the present study, do we find relations which even approximate to a 4th power law when considering the L – σ relation for Hα. It is reasonable to suppose that Hα will be even less subject than Hβ to any internal dust extinction effects, and that of the two indicators it should be the better one for total luminosity. One should bear in mind that observers in the early 1980's used Hβ for reasons of detector sensitivity, while now the situation is reversed.

The data plotted in Fig. 6 do not, if taken as a set, lend themselves to any meaningful linear fit, but the upper envelope is well fitted by the relation:

$$\log L_{\mathrm{env}} = 2.6 \log \sigma + 36.15. \quad (2)$$

As we saw in Sect. 4 above, the slope of this relation is also the slope of the observational relations $L - \sigma$ for the regions of highest surface brightness and for regions with supersonic values of sigma and with symmetric single – peaked emission profiles. These observations, coupled with our previous work on the properties of the most luminous H II regions in spirals (Rozas et al. 1997; Beckman et al. 1998) give us the leads to a physical interpretation. In Beckman et al. (1998) we showed that above a critical value L_{Str} for the Hα luminosity, there is a change in the collective and individual photometric properties of H II regions, which we ascribe to the transition from ionization bounding to density bounding, giving our theoretical and observational reasons for reaching this inference. The value of L_{Str}, which shows relatively little variance among the galaxies we have observed, is $10^{38.6}$ erg s^{-1}. The H II regions in Fig. 6 which lie on the upper envelope described by Eq. 4 have luminosities higher than this value which implies that they are density bounded. One corollary of this is that the Hα luminosity observed does not correspond to the full ionizing luminosity of the stars within the region, since a fraction of these photons escapes from the cloud. We would therefore not expect a 4th power relation between Hα (or Hβ) luminosity and σ for these regions. However, another corollary is that the H II region observed is in fact the whole placental cloud which gives birth to the ionizing stars, so the Hα luminosity $L_{\mathrm{H}\alpha}$ should be proportional to the mass of the cloud. Starting with the virial theorem in its basic form:

$$v^2 = \frac{GM}{r_{\mathrm{g}}} \quad (3)$$

where v is a characteristic internal velocity, in this case sampled via σ, M is the mass of the cloud, r_{g} is a characteristic radius, and G the gravitational constant. In order to convert Eq. 3 into a relation between $L_{\mathrm{H}\alpha}$ and σ we also need to be able to relate $L_{\mathrm{H}\alpha}$ and r_{g}. In Rozas et al. (1997) we examine the internal brightness gradients of individual luminous H II regions, showing that for $L < L_{\mathrm{Str}}$ these are invariant, corresponding to a linear relationship between luminosity and volume, but that at $L = L_{\mathrm{Str}}$ they show a jump to higher values, and a systematic linear increase for $L > L_{\mathrm{Str}}$. These observations give us an indirect clue to the behaviour of r_{g}, but since r_{g} is not just the luminosity bounded radius of a region, we cannot use our observations directly to measure its dependence on L. To parametrize

this we let $r_{\rm g}$ vary as $L_{\rm H\alpha}^{1/n}$. For the ionization bounded case, where $L < L_{\rm Str}$, $L_{\rm H\alpha}$ varies linearly with the observed volume of a region, so that if the observed emitting radius, r, were really the equivalent of the gravitational radius $r_{\rm g}$ we would for this range of L have $n = 3$. However for $L > L_{\rm Str}$, L will certainly not be 3; as a region becomes more luminous and more massive one would predict that the geometry will tend to become increasingly compact, so that n will tend to take a value larger than 3. In the first instance we will leave n as a free parameter, which we will be able to infer from the observations. Substituting for M proportional to L and $r_{\rm g}$ proportional to the power of $1/n$ in Eq. 3 we find:

$$L_{\rm H\alpha} = k\sigma^{2n/(n-1)} \tag{4}$$

where k is a constant. Eq. 4 signifies that density-bounded H II regions which are virialized will obey an $L - \sigma$ relation which will in general be less steep than a fourth power law. For example if n were 3 the exponent in Eq. 4 would also be 3. Our observational value of 2.6 in fact corresponds here to a value of 4.3 for n.

We now introduce the hypothesis which enables us to explain the observations presented in Figs. 6,7: that the H II regions on the upper envelope of Fig. 6, and also those sampled in Fig. 7 show line widths corresponding to virialization, while the other line profiles observed do not. The physical basis for this is the assumption that the line width observed in a region is due to the superposition of different velocity fields; in general the energy to sustain these will be injected from individual events, and the average profile will be a superposition of the velocity fields of these events on the general background dispersion of the region. The fraction of the emission observed which comes from sources of high velocity dispersion: the winds of massive stars, and supernovae, will depend on the fraction of the total luminous gas which participates in these events and the damping time for gasesous expansion within a given region. Both of these should fall with increasing gas mass, i.e. with increasing H II region luminosity. In the limit where the fraction of the high velocity dispersion gas tends to zero we should observe a region with virialized internal motions reflected in the velocity dispersion.

The question of whether the velocity dispersions of H II regions in general show virialization receives the general answer "no", but it should be possible to pick out those regions showing virial dispersion given measurements of dispersion, σ, for the complete population of regions in a galaxy. Assuming that the regions on the upper envelope of Fig. 6 are virialized, the measured slope of 2.6 for this envelope yields a value close to 4 for n. This is plausible, but as we have no other way to obtain n observationally, we cannot at this stage make further claims. Additional support for the underlying hypothesis can, however, be drawn from a preliminary study of M101 using the same technique as that described here (Beckman et al. 1998). The $L_{\rm H\alpha} - \sigma$ plot for M101 shows an upper envelope with a slope of 2.65 ± 0.2, in complete agreement with the value shown here for M 100, within the limits of observational error.

Table 1. Masses of individual H II regions on the upper L–σ envelope; column 1: region identifier; columns 2, 3: coordinates of region in pixels; column 4: mass ($M_\odot$) computed using the virial expression in Eq. 5: column 5: mass (M_{odot}) computed assuming density bounding, from measured luminosity of the region.

$Region$	x	y	$Mass(virial)$	$Mass(luminosity)$
1	20	302	0.116E+06	0.65E+05
2	27	579	0.797E+05	0.29E+05
3	20	329	0.869E+06	0.11E+06
4	30	301	0.115E+07	0.32E+06
5	61	244	0.159E+06	0.82E+05
6	78	229	0.158E+06	0.76E+05
7	138	449	0.118E+07	0.36E+06
8	157	447	0.837E+06	0.11E+06
9	167	468	0.138E+06	0.66E+05
10	205	448	0.117E+07	0.49E+06
11	208	454	0.780E+05	0.12E+05
12	210	107	0.108E+07	0.46E+06
13	246	80	0.136E+07	0.32E+06
14	284	418	0.216E+06	0.46E+05
15	326	294	0.497E+06	0.18E+06
16	333	456	0.154E+06	0.89E+05
17	338	271	0.171E+06	0.79E+05
18	355	158	0.228E+06	0.51E+05
19	404	167	0.423E+06	0.10E+06
20	408	392	0.909E+05	0.206E+05

There is a way in which we can check the validity of our hypothesis about which H II regions are in fact virialized. The virial theorem allows us to compute the mass of a virialized region using the formula:

$$M = \frac{3\sigma^2 r_{\rm g}}{G} \tag{5}$$

which is an approximation based on Eq. 3 and the definition of $r_{\rm g}$, from Tenorio-Tagle et al. (1993). However, as the regions with luminosities greater than $L_{\rm Str}$ are density bounded, a measurement of the luminosity of a region in this range of L, combined with an estimate of its density using electron density as the observable, enables us to make an independent estimate of its mass. Density bounding implies that the mass of ionized gas in a region should be the same as the mass of the whole placental cloud in which its ionizing star cluster has formed. The results of this exercise for specific regions in M 100 are given in Table 1.

The electron densities for these regions have not in fact yet been measured, and we have taken generic global mean values based on direct measurements in other galaxies (see e.g. Rozas et al. 1996) , where we have found that variations of more than a factor two in the electron densities of high luminosity regions are not found, so that the masses estimated by equating the atomic number density to the electron number density, integrating over the volume of the region, and allowing an increment in mass for helium, will be good to within a factor of around 2. Likewise the compactness of a region in terms of its mass distribution

Table 2. Masses of the individual H II regions chosen to be well below the L–σ envelope. The "virial" masses here are an order of magnitude higher than the luminosity masses. Columns designations as in Table 1.

$Region$	x	y	$Mass(virial)$	$Mass(luminosity)$
1	29	555	0.255E+05	0.25E+04
2	178	517	0.292E+05	0.50E+04
3	211	514	0.563E+05	0.48E+04
4	212	531	0.165E+05	0.24E+04
5	242	520	0.159E+05	0.38E+04
6	427	346	0.178E+05	0.29E+04
7	441	372	0.418E+05	0.66E+04
8	510	386	0.248E+05	0.45E+04
9	556	440	0.197E+05	0.10E+04
10	572	526	0.480E+05	0.29E+04

is not easy to assess from the measurements we have, so that the factor 3 in Eq. 5 is in fact likely to vary somewhat with the mass of the region. With these uncertainties taken into account the agreement between the masses of regions determined by these different techniques is fair. The mass derived from the luminosity is consistently lower than the virial mass by a factor of some 2–3, most of which can be directly attributted to our use of an average electron density, from Rozas et al. (1996), while the values of the density for the most luminous regions tend to be higher by factors of 2.

We applied the same methods to determine the masses of the regions that are not on the upper $L-\sigma$ envelope and according to our hypothesis the σ's observed should not be the virial σ's for the regions concerned. In Table 2, we give a comparison between the results of the two techniques for the masses also in these cases, and we find that the "virial" masses are much greater than the luminosity masses. This is consistent with the hypothesis that their sigmas are larger than virial, and supports our choice of only the envelope regions as exhibiting virialized σ's.

A corollary of this result is that if one wishes to measure the masses of an H II region using the virial theorem, one must select the value of σ in Eq. 4 as the value of the intercept of the locus of constant L for the region measured with the $L-\sigma$ envelope for the full set of regions. This technique will work really well only for the density – bounded regions, with $L > L_{\rm Str}$, but could be adapted for regions of lower luminosity, given measurements of sufficient resolution in velocity.

6. Concluding remarks

We have used the TAURUS Fabry-Perot instrument to obtain velocity images in Hα emission of the disc of the grand design spiral M 100 (NGC 4321). We have analyzed the internal velocity fields of the 200 H II regions most luminous in Hα, which were calibrated in luminosity using the photometric Hα intensity map of Knapen (1998). The emission spectra of individual regions were analyzed, and will be published electronically through the CDS as a complement of this paper. In the present study we have concentrated on the question of whether the emission lines reflect internal velocity dispersions of H II regions which would be predicted from the virial theorem. The briefest summary answer is "no, in general they do not", and this conclusion could already have been drawn from a previous paper by Arsenault et al. (1990). However our graph of velocity dispersion versus luminosity, for the highest range of luminosities, shows a linear envelope in the $\log-\log$ plane, which we attribute to regions which are in fact virialized. Regions with the same luminosities but higher measured internal velocity dispersions than those on the locus of this envelope are displaying line profiles which reflect the presence of as yet undamped individual high energy events (stellar winds, even supernovae). Support for this hypothesis is provided by the observation that profiles with the highest measured line widths are not found in the most luminous regions. This is what one would expect if both volume averaging and time averaging were contributing to the profiles observed. In the most luminous regions, an individual high velocity event will provide a lower fraction of the total luminosity, and will also be damped more rapidly within the high gas mass of the region.

The slope of the linear envelope in the $\log L - \log\sigma$ plane for the regions which we claim to be virialized is found to be 2.6, rather than taking a value 4 as predicted theoretically. However, as shown in Beckman et al. (1998), regions with Hα luminosities greater than a critical value of $10^{38.6}$ erg s^{-1} are, in general, density bounded; the regions on the envelope are all in this high luminosity range. For these regions a fraction of the total luminosity emitted by the stars exciting the region escapes without contributing to the observed Hα luminosity, and this fraction is an increasing proportion of the total as the luminosity increases. If the measured Hα luminosity is used as the observable parameter, the index of its dependence on σ will therefore be less than 4, and we have shown here that a value of 2.6 is physically plausible.

For a density bounded region, the total mass of gas can be estimated directly from the Hα luminosity, and then compared with the mass computed assuming that the virial theorem holds. We show here that the masses derived by the two different methods are comparable for the regions on the $\log L-\log\sigma$ envelope; by contrast the "virial" masses are much too high for the other regions. We infer that it is possible to use the virial theorem to obtain H II region masses only if we are able to obtain a complete data set for a galaxy, which enables us to derive the appropiate $\log L - \log\sigma$ envelope. Even in this case relatively reliable masses are measurable only for the regions on the envelope. On the other hand the masses of all the high luminosity regions, those which $\log L_{H\alpha} > 38.6$ (erg s^{-1}), can be found by integrating over the measured Hα surface brightness (which can be used to infer a mean electron density) since these are fully ionized by their OB stellar populations.

This study has been restricted to one galaxy, but we do have a similar data set for M101 without absolute flux calibration, and as shown in Beckman et al. (1998) the $\log L - \log\sigma$ diagram is very similar to that for M 100, and in particular there is a well defined linear upper envelope with gradient close to 2.55, and there are more cases of high luminosity-weighted average ve-

locity dispersion for individual regions with lower luminosities. Since we have evidence of different types for the property of density bounding for the most luminous H II regions in a number of other galaxies, (Rozas et al. 1996; Beckman et al. 1998) it will be rewarding to carry out a full statistical survey of their internal velocity dispersions and profiles using the same rather efficient Fabry-Perot method which has given us the present results.

Acknowledgements. The William Herschel Telescope is operated on the island of La Palma by the Royal Greenwich Observatory in the Spanish Observatorio del Roque de los Muchachos of the Instituto de Astrofísica de Canarias. This work was partially supported by the Spanish DGICYT (Dirección General de Investigación Científica y Técnica) via Grants PB91-0525 and PB94-1107. This research has made use of the NASA/IPAC Extragalactic Database (NED) which is operated by the Jet Propulsion Laboratory, California Institute of Technology, under contract with the National Aeronautics and Space Administration.

References

Arsenault R., Roy J. R., Boulesteix J. 1990, A&A 234, 23
Beckman, J. E., Peletier, R. F., Knapen, J. H., Corradi, R. L. M. & Gentet, L. J. 1996, ApJ 467, 175
Beckman, J. E., Rozas, M., Knapen, J. H. & Zurita, A. 1998, ApJ, submitted
Cepa, J. & Beckman, J. E. 1990, A&AS 83, 211
Hanes, D. A. 1982, MNRAS 201, 150
Kennicutt R.C. 1979a, ApJ 228, 394
Kennicutt R. C. 1979b, ApJ 228, 696
Kennicutt R. C. 1979c, ApJ 228, 704
Kennicutt R.C. 1981, ApJ 247, 9
Knapen, J. H. 1996, in Proc. Nobel Symposium 98 *Barred Galaxies and Circumnuclear Activity*, Eds. Aa. Sandqvist, P.O. Lindblad, Lecture Notes in Physics, 474, 233, Springer-Verlag, Berlin
Knapen, J. H., Beckman, J.E., Cepa, J., van der Hulst, J.M. & Rand, R.J. 1992, ApJL 385, L37
Knapen, J. H., Cepa, J., Beckman, J. E., del Rio, M. S. & Pedlar, A. 1993, ApJ 416, 563
Knapen, J. H., Beckman, J. E., Shlosman, I., Peletier, R.F., Heller, C.H. & de Jong, R.S. 1995a, ApJL 443, L73
Knapen, J. H., Beckman, J. E., Heller, C.H., Shlosman, I. & de Jong, R.S. 1995b, ApJ 454, 623
Knapen, J. H., & Beckman, J. E. 1996, MNRAS 283, 251
Knapen, J. H., Beckman, J. E., Cepa, J. & Nakai, N. 1996, A&A 308, 27
Knapen, J. H. 1998, MNRAS, submitted
Knapen, J. H., Rozas, M. & Beckman, J. E. 1999, in preparation.
Medina Tanco, G. A., Sabalisck, N., Jatenco-Pereira, V. & Opher, R. 1997, ApJ 487, 163
Melnick, J. 1979, ApJ 238, 112
O'Dell, C.R., Townsley 1988, A&A, 198, 283
Osterbrock D. E. 1989, *Astrophysics of Gaseous Nebulae and Active Galactic Nuclei*, Mill Valley, CA, University Science Books.
Rozas, M., Beckman, J. E. & Knapen, J. H. 1996, A&A 307, 735
Rozas, M., Castañeda, H. O. & Beckman, J. E. 1998, A&A 330, 873
Sandage A. 1962, ApJ 136, 319
Sandage, A. & Tammann, G.A. 1974, ApJ 190, 525
Sersic, J. L. 1960, Zs.f. Ap 50, 168
Tenorio-Tagle, G., Muñoz-Tuñon, C., Cox, P.D. 1993, ApJ, 418, 767
Terlevich, R. & Melnick, J. 1981, MNRAS 195, 839
van der Bergh, S. 1980, ApJ 235, 1